Supplementary Information

Engineered Flexible Microsupercapacitors with MOF-Derived Co₃O₄/rGO Nanocomposite Optimized via Response Surface Methodology for Enhanced Energy Storage

Mohammad Saquib [a], Shilpa Shetty [a], S.G Siddanth [b], Nagaraj Nayak [a], Chandra Sekhar Rout [c], Ramakrishna Nayak [d], Ahipa T. N [e], M. Selvakumar [a†]

[a] Department of Chemistry, Manipal Institute of Technology, Manipal Academy of Higher Education, Manipal-576104, Karnataka, India.

[b] Department of Chemical Engineering, Manipal Institute of Technology, Manipal Academy of   Higher Education, Manipal, 576104, Karnataka, India

[c] Department of Chemical Engineering, Chungbuk National University, Cheongju, Chungbuk 28644, Republic of Korea

[d] Department of Humanities and Management, Manipal Institute of Technology, Manipal Academy of Higher Education, Manipal, 576104, Karnataka, India

[e] Centre for Nano and Material Sciences, Jain (Deemed-to-be University), Jain Global Campus, Kanakapura, Bangalore, Karnataka, 562112 India

Correspondence†: M Selvakumar **(selva.kumar@manipal.edu)**

1. Structural and elemental characterization

1.1. Material Characterizations and Methodology

The chemicals utilized in this research were sourced from renowned chemical vendors. Specifically, LOBA Chemie PVT. LTD provided Graphitic carbon powder (C), Cobalt (II) nitrate hexahydrate ($Co(NO_3)2 \cdot 6H_2O$), 2-Methylimidazole (2-MIM) ($C_4H_6N_2$), Concentrated orthophosphoric acid (H_3PO_4), sulphuric acid (H_2SO_4), Potassium permanganate ($KMnO_4$) and solvents such as Methanol (CH_3OH), Acetone (CH_3)2CO (98%), and Diacetone alcohol ($C_6H_{12}O_2$, 98%). Additionally, Cellulose acetate propionate ($C_{76}H_{114}O_{49}$) was procured from Sigma-Aldrich. All these materials were used as received without further purification.

The nanomaterials' phase composition was examined using a Rigaku Miniflex 600 X-ray diffractometer. This analysis utilized Cu Kα radiation with a wavelength of 0.1542 nm, operating at 40 kV and 15 mA. Diffraction data were collected across a 5° to 60° range, with a

scanning speed of 2° per minute. AFM data were processed using Gwyddion software (version 2.47). X-ray photoelectron spectroscopy (XPS) was performed on the synthesized composite using an ESCALAB 250xi instrument from Thermo-Scientific, equipped with a Micro-focused Monochromator. The analysis employed Al Kα X-ray radiation to investigate the elemental distribution and surface chemical composition. The XPS spectra were deconvolved using a Gaussian-Lorentzian mixture model in Origin software. For morphological examination, a Scanning Electron Microscope (SEM) from Carl Zeiss was employed. Electrochemical performance evaluations were carried out using a Biologic SP-50e electrochemical workstation, employing techniques such as Electrochemical Impedance Spectroscopy (EIS), Cyclic Voltammetry (CV), and Galvanostatic Charge-Discharge (GCD). CV measurements were conducted in a potential window of 0 to 1 V at a scan rate of 5 mVs^{-1}. GCD tests were performed within the same potential window, with varying current densities, including 5 mAcm^{-2}. EIS was performed using an AC voltage of 0.05 V amplitude, across a frequency range from 1 MHz to 100 mHz. The viscosity and surface tension of the conductive inks were measured using an advanced modular rheometer instrument. The contact angle of the ink droplets on the substrate was determined using an Ossila goniometer, with measurements spanning from 0° to 180°. Finally, symmetric and asymmetric microsupercapacitors were fabricated and tested in a two-electrode configuration, with the prepared nanocomposite serving as one electrode and activated carbon as the counter electrode.

$$D = (\frac{K\lambda}{\beta Cos\theta})$$

(1)

$$\delta = \frac{1}{D^2}$$

(2)

$$\varepsilon = \frac{FWHM}{4\tan\theta}$$

(3)

Table S1 Detailed tabulated data showing the specific surface area (SSA), total pore volume, and average pore diameter of the prepared electrode material at different calcination temperatures

Samples	Temperature (°C)	Specific surface area [m^2 g^{-1}]	Total pore volume [cm^3 g^{-1}]	Average pore diameter [nm]
CR-1	350	87.194	0.00158	0.6999
CR-2	450	183.10	0.09306	1.0165
CR-3	550	614.13	0.33490	0.7648

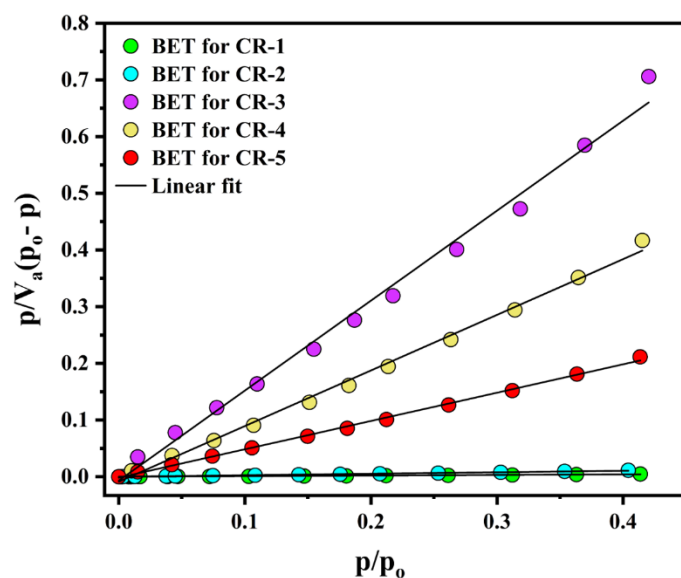| CR-4 | 650 | 9.3670 | 0.00515 | 0.1026 |
| CR-5 | 750 | 5.1337 | 0.00263 | 0.0131 |

1.2. BET analysis

Figure S1. shows the specific surface area of the electrode material (CR-1 to CR-5) calcined at various temperatures (350°C to 750°C).
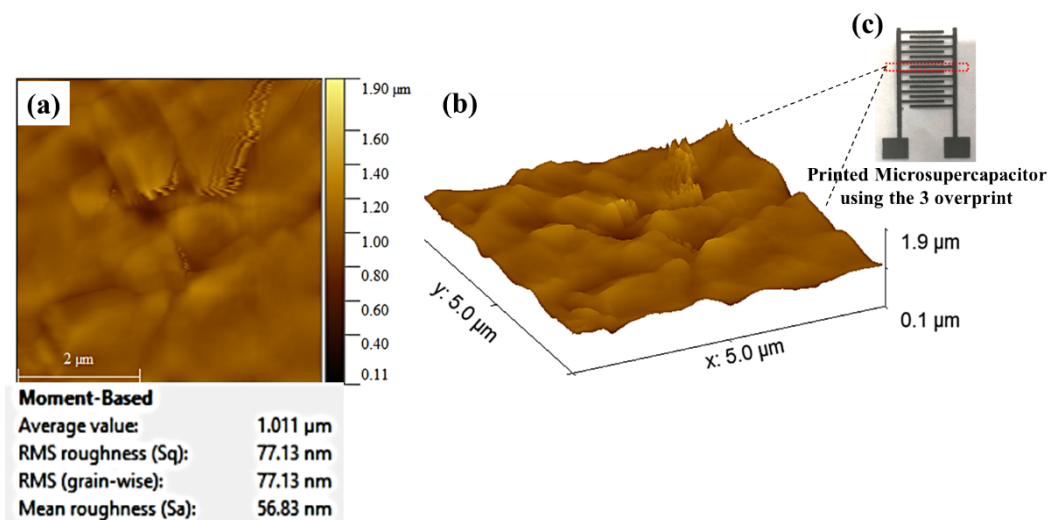
1.3. AFM analysis

Figure S2. AFM analysis of printed Co_3O_4/rGO composite device (CR-3).
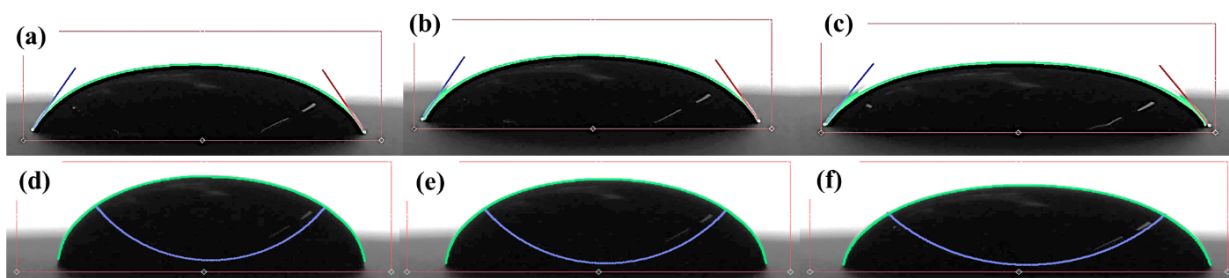
1.4. Contact angle analysis

Figure S3 (a-c). The contact angle of the conductive ink droplet over the flexible substrate, **(d-f)** Surface tension at different time intervals.

Table S2. Rs and Rct for Co_3O_4-Based Electrodes at Different Annealing Temperatures using the circuit fitting RQ(RW).

Annealing Temperature °C	Rs (Ω)	Rct (Ω)
350	8	90
450	7	75
550	5	45
650	6	55
750	10	65

Table S3. Experimental data for symmetric microsupercapacitor.

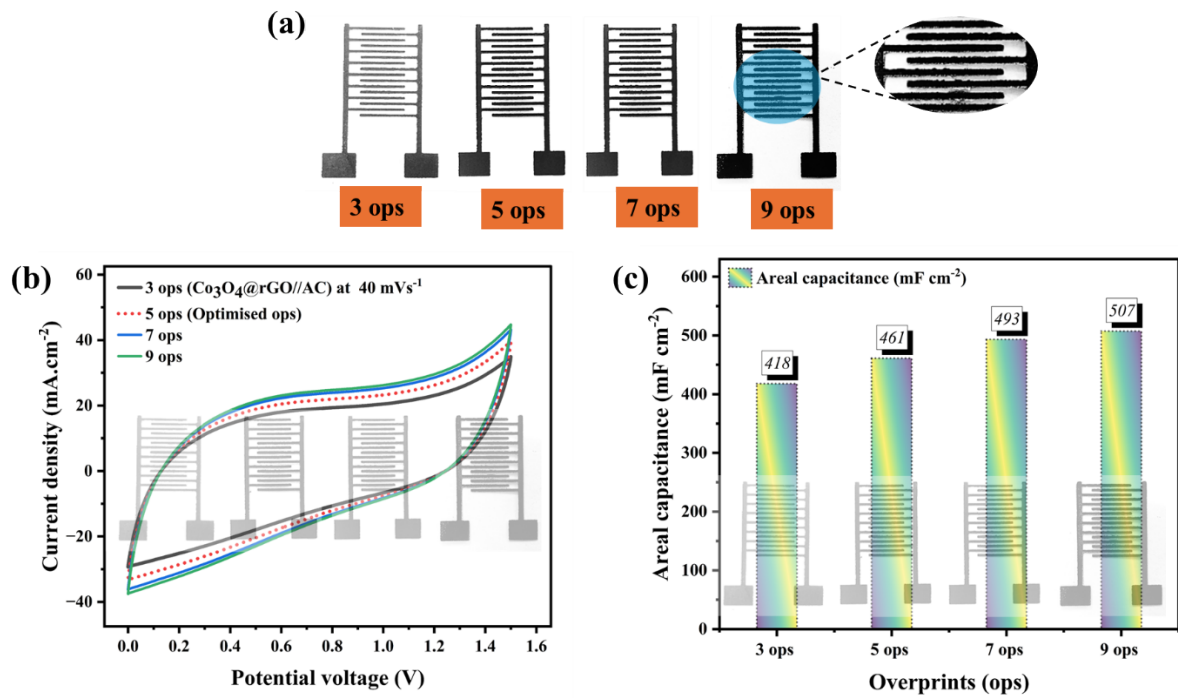| A: Temperature (°C)	B: CV cycles	Areal capacitance (mFcm⁻²)	Energy density (µWhcm⁻²)	Power density (mWcm⁻²)
350	4	554.0	76.9	2518.1
450	4	678.9	94.3	2390.4
550	4	939.0	130.4	2134.0
650	4	835.7	116.1	2334.3
750	4	751.2	104.3	2454.8

Figure S4. An illustration of the microsupercapacitor with overprints (ops), (b) CV curves of asymmetric microsupercapacitor at 40 mVs^{-1}, (c) Areal capacitance for various overprints.
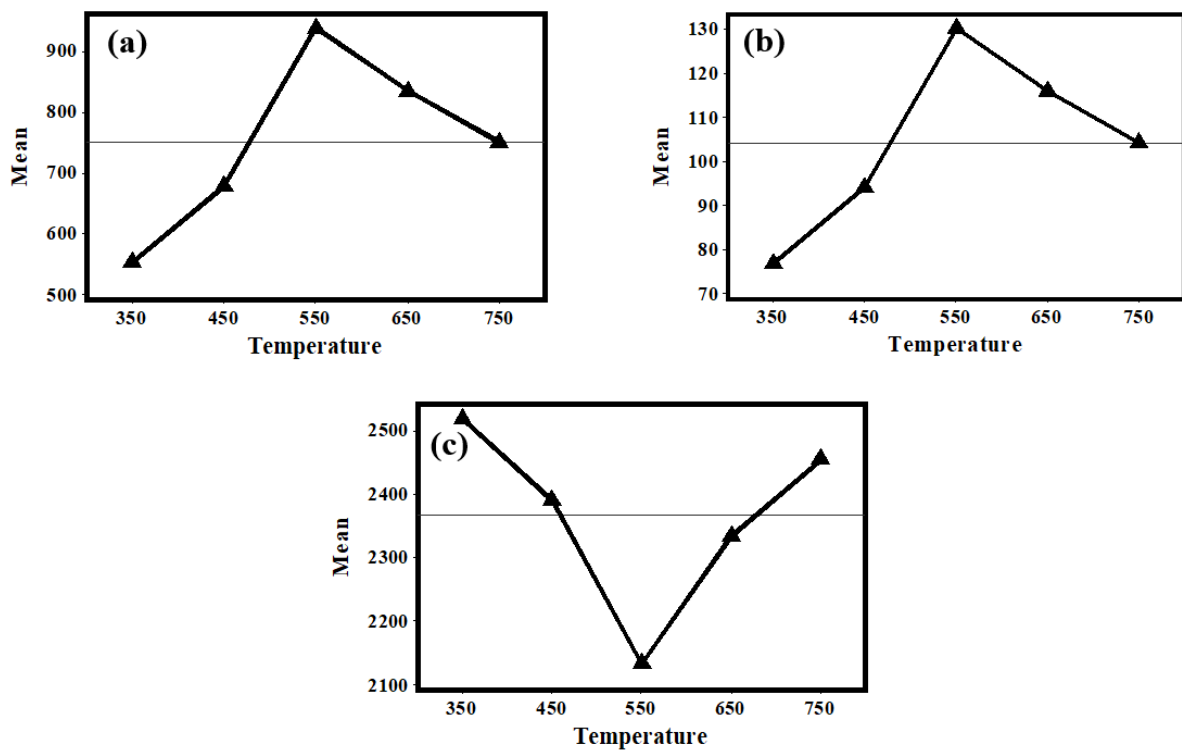
Figure S5. Main effects plot for **(a)** areal capacitance, **(b)** energy density, and **(c)** power density

Table S4. ANOVA for output parameters.

Source	DF	Seq SS	Adj SS	Adj MS	F	P
Areal capacitance						
Regression	2	74084.8	74084.4	37042.4	5.96	0.144
Linear	1	30382.1	30382.1	30382.1	4.89	0.158
Temperature	1	30382.1	30382.1	30382.1	4.89	0.158
Square	1	43702.6	43702.6	43702.6	7.03	0.118
Temperature*Temperature	1	43702.6	43702.6	43702.6	7.03	0.118
Residual Error	2	12437.9	12437.9	6218.9		
Total	4	86522.7				
S = 78.8602 R-Sq = 85.62 % R-Sq (adj) = 71.25 %						
Energy density						
Regression	2	1432.29	1432.29	716.144	6.00	0.143
Linear	1	586.76	586.76	586.756	4.91	0.157
Temperature	1	586.76	586.76	586.756	4.91	0.157
Square	1	845.53	845.53	845.531	7.08	0.117
Temperature*Temperature	1	845.53	845.53	845.531	7.08	0.117
Residual Error	2	238.87	238.87	119.436		
Total	4	1671.16				
S = 10.9287 R-Sq = 85.71 % R-Sq (adj) = 71.41 %						
Power density						
Regression	2	68223.6	68223.6	34111.8	3.74	0.211
Linear	1	3337.9	3337.9	3337.9	0.37	0.607
Temperature	1	3337.9	3337.9	3337.9	0.37	0.607
Square	1	64885.7	64885.7	64885.7	7.12	0.116
Temperature*Temperature	1	64885.7	64885.7	64885.7	7.12	0.116
Residual Error	2	18220.0	18220.0	9110.0		
Total	4	86443.6				
S = 95.4462 R-Sq = 78.92 % R-Sq (adj) = 59.85 %						

DF – Degrees of Freedom; **Seq SS** – Sequential Sum of Squares; **Adj SS** – Adjusted Sum of Squares; **Adj MS** – Adjusted Mean Square; **S** – Standard deviation of residuals

Table S5. Descriptive statistics for areal capacitance, energy density, and power density.

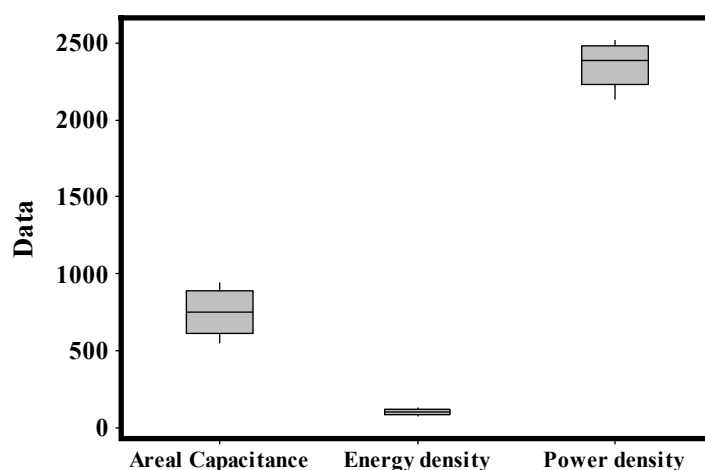| Variable	N	N^*	Mean	Standard Error of Mean	Standard Deviation	Minimum	Q1	Median	Q3	Maximum
Areal Capacitance	5	0	751.8	65.8	147.1	554.0	616.5	751.2	887.4	939.0
Energy density	5	0	104.40	9.14	20.44	76.90	85.60	104.30	123.25	130.40
Power density	5	0	2366.3	65.7	147.0	2134.0	2234.2	2390.4	2486.4	2518.1

Figure S6. Boxplots of areal capacitance, energy density, and power density.

Table S7. Experimental and design predicted values for symmetric microsupercapacitors at various calcinating temperatures.

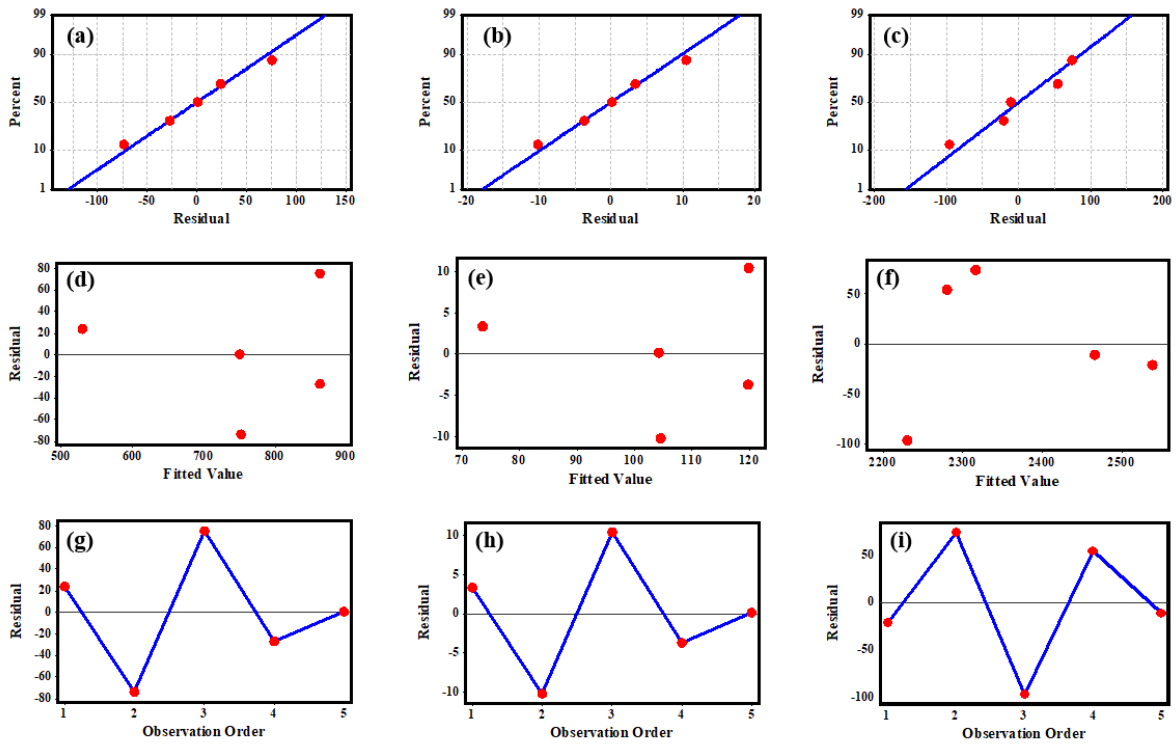| Temperature (°C)	Areal Capacitance (mF cm⁻²)		Energy density (µWhcm⁻²)		Power density (mWcm⁻²)	
	Experimental	Predicted	Experimental	Predicted	Experimental	Predicted
350	554	529.777	76.9	73.537	2518.1	2539.02
450	678.9	752.511	94.3	104.511	2390.4	2316.51
550	939.0	863.503	130.4	119.943	2134.0	2230.16
650	835.7	862.751	116.1	119.831	2334.3	2279.97
750	751.2	750.257	104.3	104.177	2454.8	2465.94

Figure S7. (a-c) Normal probability plots of areal capacitance, energy density, and power density, **(d-f)** Versus fit plots of areal capacitance, energy density, order plots of **(a)** areal capacitance, **(b)** energy density, and **(c)** power density, **(g-i)** Versus order plots for areal capacitance, energy density, and power density
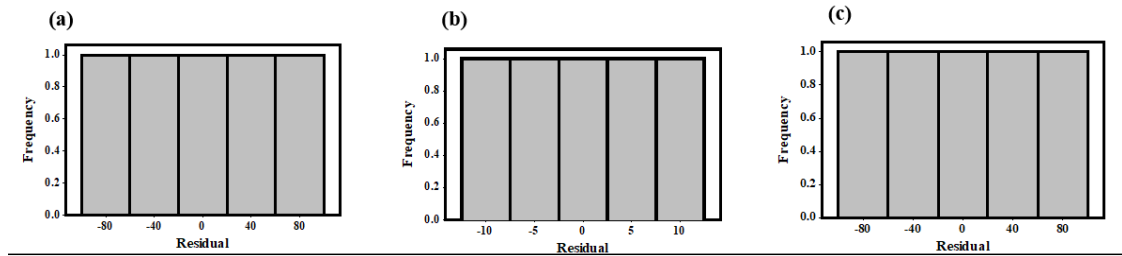

Figure S8. Histogram plots of (a) aerial capacitance, (b) energy density and (c) power density
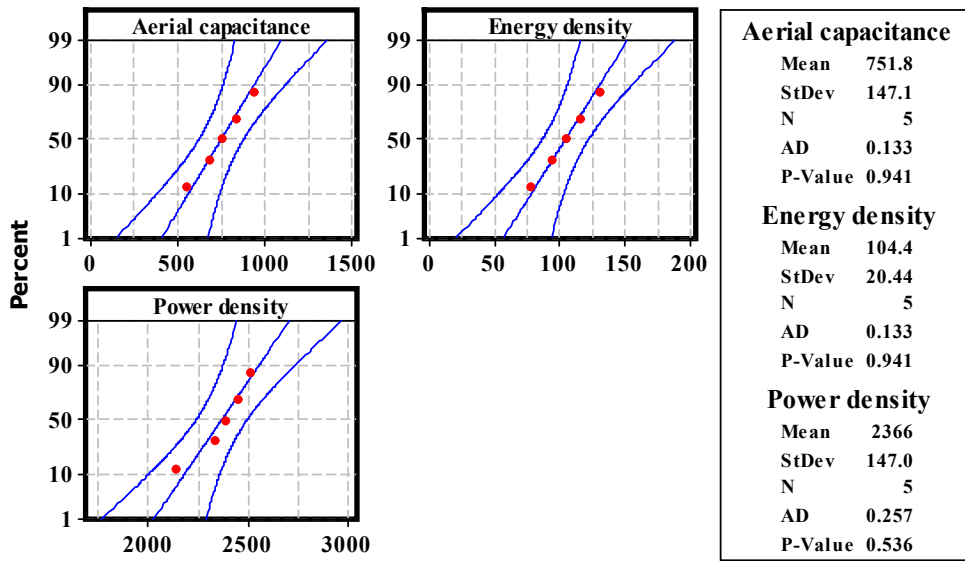
Normal - 95% CI

Figure S9. Probability plots of areal capacitance, energy density, and power density.
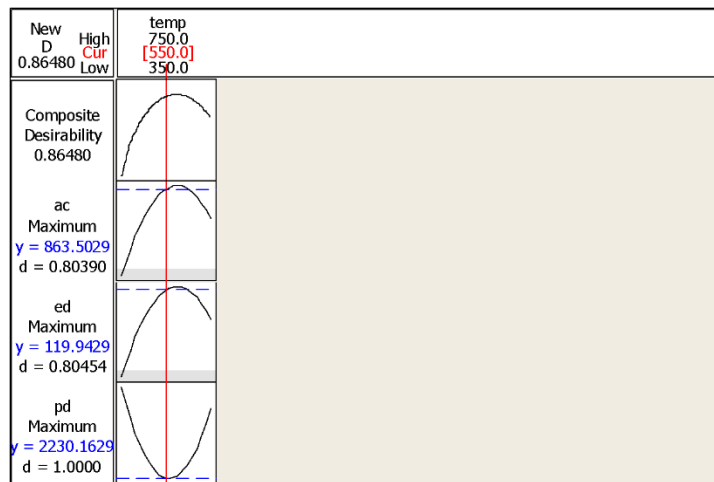

Figure S10. Optimization plots of response variables for a symmetric microsupercapacitor.

Table S7. Predicted response for design points using model for areal capacitance, energy density, and power density

Point	Fit	Standard Error of Fit	95 % CI	95 % PI
Areal Capacitance				
1	529.777	74.2173	(210.446, 849.11)	(63.835, 995.72)
2	752.511	48.0613	(545.720, 959.30)	(355.154, 1149.87)
3	863.503	54.9602	(627.028, 1099.98)	(449.920, 1277.09)
4	862.751	48.0613	(655.960, 1069.54)	(465.394, 1260.11)

5	750.257	74.2173	(430.926, 1069.59)	(284.315, 1216.20)
Energy density				
1	73.537	10.2853	(29.2833, 117.791)	(8.9654, 138.109)
2	104.511	6.6605	(75.8537, 133.169)	(49.4445, 159.578)
3	119.943	7.6166	(87.1715, 152.714)	(62.6274, 177.258)
4	119.831	6.6605	(91.1737, 148.489)	(64.7645, 174.898)
5	104.177	10.2853	(59.9233, 148.431)	(39.6054, 168.749)
Power density				
1	2539.02	89.8267	(2152.52, 2925.51)	(1975.08, 3102.96)
2	2316.51	58.1697	(2066.23, 2566.80)	(1835.58, 2797.44)
3	2230.16	66.5195	(1943.95, 2516.37)	(1729.60, 2730.73)
4	2279.97	58.1697	(2029.69, 2530.26)	(1799.04, 2760.90)
5	2465.94	89.8267	(2079.44, 2852.43)	(1902.00, 3029.88)